Supplementaries for 'Reshaping Wi-Fi ISAC with High-Coherence Hardware Capabilities'

Zhiping Jiang

1 Introduction

This supplement extends our main manuscript "Reshaping Wi-Fi ISAC with High-Coherence Hardware Capabilities," offering detailed comparison on non-coherent versus coherent CSI in Section 2, and explanations for some capabilities in Section 3.

Research on high-coherence hardware capabilities is an ongoing endeavor. We provide a dedicated page `https://ps.zpj.io/reshaping-wifi-isac.html` to provide continuous updates on this topic. This page will serve as a repository for the latest information on our findings and the evolving capabilities related to this transformative work in Wi-Fi ISAC.

2 Non-coherent CSI vs. Coherent CSI

In this section, we provide a detailed comparative analysis of non-coherent versus coherent CSI measurements. This comparison is pivotal for illustrating the advantages of high-coherence capabilities. However, due to the magazine's constraints on length, we are unable to include these images in the main body of the text. For the sake of brevity in our discussion, we use the abbreviations *NCH* for non-coherent and *CH* for coherent.

2.1 Experiment Setup

For NCH CSI, we use the PicoScenes platform to control two Intel AX210 NICs for the transmission and reception of 802.11ax-format frames over a 20 MHz channel. To prevent environmental interference, we use double-layer shielded SMA cables and a 20 dB attenuator to connect the transmitting (Tx) and receiving (Rx) antennas directly.

For CH CSI, we transmit 802.11ax frames using two NI USRP B210 devices over the same cable-connected channel. Unlike the NCH setup, in this configuration, frames are transmitted in Batch Tx mode using the Batch Tx API provided by PicoScenes platform. In the Batch Tx mode, the PPDUs (the baseband signals of the frame) are pregenerated and stringently spaced with a user-specified interval, *e.g.*, 100μs. These PPDUs are then concatenated and transmitted in a single burst.

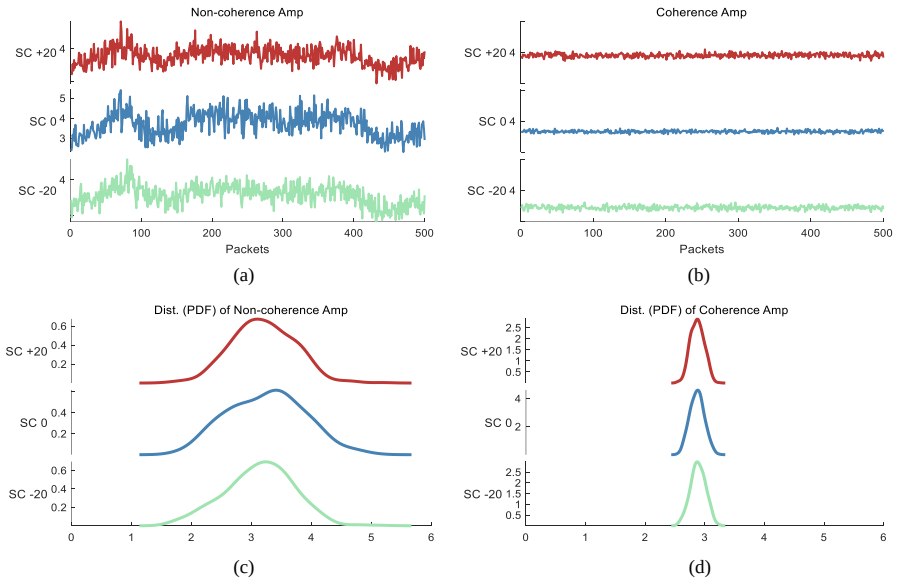

Figure 1: Comparison of non-coherent and coherent CSI in amplitude.

2.2 Result Analysis

Figures 1, 2, and 3 present a comparison between NCH and CH CSI in terms of amplitude, phase from a single subcarrier, and STO, respectively. In the following sections, we provide a detailed analysis of each aspect.

2.2.1 Amplitude Analysis

Figure 1(a) and (b) show the amplitude responses of the -20th, 0th, and 20th subcarriers across 500 consecutively received frames. Figure 1(c) and (d) depict the corresponding probability density function (PDF) outputs. The comparison reveals that the amplitudes measured by the NCH method exhibit a large variance, whereas the CH amplitudes demonstrate remarkably stable measurements with minimal variance.

It is critical to note that in both experiments, the Tx and Rx units were cable-connected and well-shielded. Therefore, the large variation observed in the NCH amplitude can be solely attributed to the intrinsic dynamics of the commercial Wi-Fi NICs. Specifically, this variability arises from the six CODEs, which are elaborated in Section III of the main text.

The CH amplitude shows remarkable stability, displaying only minimal variance. This consistency is attributed to several factors. First, the Tx power for all frames was consistently maintained, and the Rx gain was kept constant. Furthermore, the filters at both ends remained unchanged throughout the experiment.

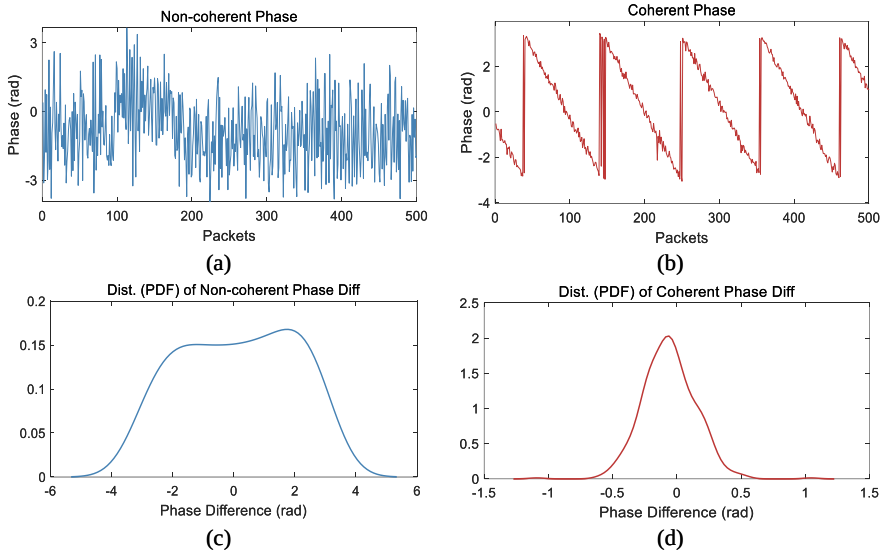

Figure 2: Comparison of non-coherent and coherent CSI in phase.

2.2.2 Phase Analysis

Figure 2(a) and (b) present the phase values of the 0th subcarrier measured across 500 consecutively received frames. The PDF of the phase differences between successive measurements is depicted in Figure 2(c) and (d). The phase measured using the NCH method exhibits significant noise, with phase measurement differences characterized by a uniform distribution over the range $[-\pi, \pi]$. In contrast, the phase measured using the CH method reveals a striking sawtooth-shaped pattern. This pattern represents a novel observation that, to our knowledge, has not been documented in previous studies. Furthermore, the phase differences in the CH scenario follow an unusual normal distribution.

The distribution of the NCH phase has been thoroughly investigated and comprehensively explained in previous research. It is well-established that CFO can lead to considerable accumulative phase errors, which account for the observed large variations in phase on a per-frame basis. Additionally, due to phase wrapping, the aggregate distribution of phase differences typically manifests as a uniform distribution.

The sawtooth pattern observed in the CH phase can be attributed to the precise timing synchronization achieved by TIME capability. With TIME, we can specify the IFS with sample-level accuracy, ensuring that each frame is consistently spaced apart in time. This precise timing control results in a fixed accumulation of phase errors associated with the CFO, producing the distinctive sawtooth pattern observed in the CH phase data.

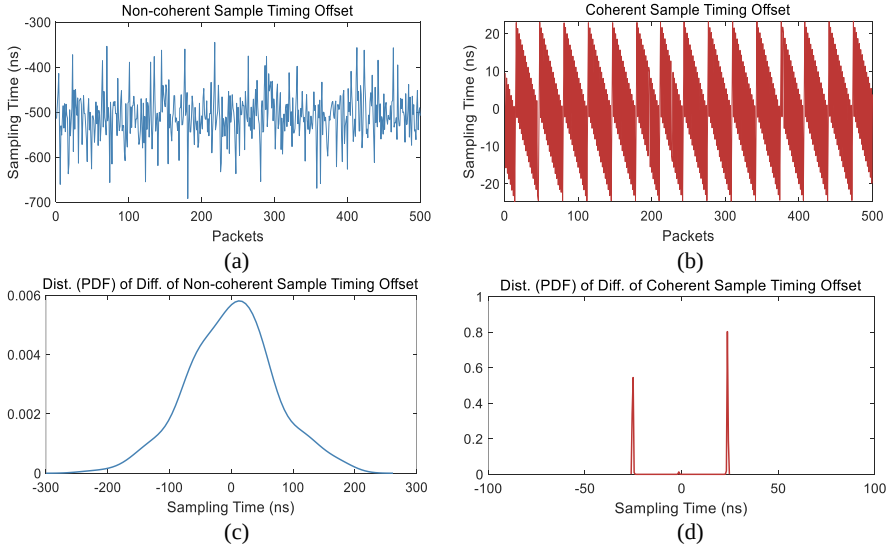

Figure 3: Comparison of non-coherent and coherent CSI in STO.

2.2.3 STO Analysis

Figure 3(a) and (b) display the variations in STO extracted from 500 consecutively received frames. The corresponding PDFs of the STO differences are depicted in Figure 3(c) and (d). The NCH STO demonstrates considerable noise and adheres to a normal distribution. In contrast, the CH STO displays a sawtooth-shaped pattern and exhibits a multi-modal normal distribution, which closely resembles the CH phase data.

NCH STO's distribution has been extensively examined and well explained in earlier studies. SFO is responsible for the accumulation of timing errors, which in turn contributes to the variability in the per-frame STO.

For the CH STO, the sawtooth-shaped pattern emerges due to the precise timing synchronization achieved by TIME. With TIME, we can specify the IFS with sample-level accuracy, ensuring that each frame is consistently spaced apart in time. This precise timing control results in a fixed accumulation of STO, producing the distinctive sawtooth pattern observed in the CH STO data.

3 Additional Explanations for Proposed Capabilities

- CMM: Rx should be capable of measuring CSI in monitor mode for *all* hardware-supported OFDM formats, *i.e.*, NonHT, HT, VHT, HE, and EHT.
- DPLR: By specifying HE LTF-Type=1, Midamble Interval=10 and SISO mode, it is possible to insert up to 39 HE-LTFs within a 5.484ms long PPDU.
- PILO: A Wi-Fi PPDU consists of multiple OFDM symbols. Through these OFDM

symbols, certain subcarriers are used for inter-symbol calibration, *i.e.*, Pilot subcarriers. Researchers can utilize the raw pilot subcarriers to re-construct Pilot subcarrier-based CSI, which enables more precise estimation for CFO and SFO.

- TIME: This capability has two levels of timing requirements. First, Tx should be capable of transmitting a PPDU at a given time with sample-level accuracy. Second, Tx should be capable of transmitting a batch of PPDUs with user-specified IFSs.
- PCOD: Vendors should provide API to allow user to specify the precoding matrix, which is structured as $N_{Tone} \times N_{STS} \times N_{tx}$, where N_{Tone}, N_{STS}, and N_{tx} denote the number of subcarriers, the number of space-time streams, and the number of tx antennas, respectively.
- TUNE: Vendors should provide API to allow user to modify the carrier frequency arbitrarily, or fine-tune the carrier frequency within a range.
- SMLO: With this capability, two independent front-end modules can operate like a time-synchronized Tx-Rx pair, supporting mono-static mode sensing.